JCTC Journal of Chemical Theory and Computation

pubs.acs.org/JCTC Article

Ideal Conductor Model: An Analytical Finite-Size Correction for Nonequilibrium Molecular Dynamics Simulations of Ion Transport through Nanoporous Membranes

Brian A. Shoemaker, Tiago S. Domingues, and Amir Haji-Akbari*

Cite This: J. Chem. Theory Comput. 2022, 18, 7142−7154 Read Online

ACCESS | Metrics & More | Article Recommendations | Supporting Information

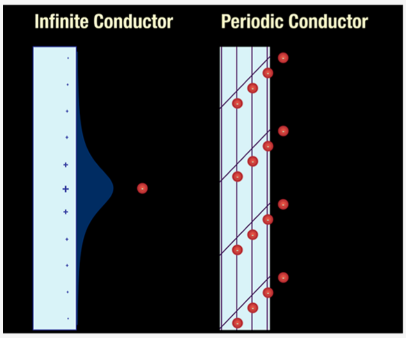

ABSTRACT: Modulating ion transport through nanoporous membranes is critical to many important chemical and biological separation processes. The corresponding transport timescales, however, are often too long to capture accurately using conventional molecular dynamics (MD). Recently, path sampling techniques, such as forward-flux sampling (FFS), have emerged as attractive alternatives for efficiently and accurately estimating arbitrarily long ionic passage times. Here, we use non-equilibrium MD and FFS to explore how the kinetics and mechanisms of pressure-driven chloride transport through a nanoporous graphitic membrane are affected by its lateral dimensions. We not only find ionic passage times and free energy barriers to decrease dramatically upon increasing the membrane surface area but also observe an abrupt and discontinuous change in the locus of the transition state. These strong finite size effects arise due to the cumulative effect of the periodic images of the leading ion entering the pore on the distribution of the induced excess charge at the membrane surface in the feed. By assuming that the feed is an ideal conductor, we analytically derive a finite size correction term that can be computed from the information obtained from a single simulation and successfully use it to obtain corrected free energy profiles with no dependence on the system size. We then estimate ionic passage times in the thermodynamic limit by assuming an Eyring-type dependence of rates on barriers with a size-independent prefactor. This approach constitutes a universal framework for removing finite size artifacts in molecular simulations of ion transport through nanoporous membranes and biological channel proteins.

1. INTRODUCTION

Membranes are crucial for maintaining stable steady states within compartmentalized systems by modulating the transport of different molecules and ions.[1] Examples include biological cells, organelles, and industrial separation processes, such as water desalination and liquid and gas separation. What determines a membrane's efficacy in all such applications is its selectivity, that is, its ability to preferentially impede the passage of certain chemical entities.[2−4] How a membrane's molecular structure impacts its selectivity, however, is far from fully understood, mostly due to the inability of existing experimental techniques in the molecular-level probing of solute transport through membranes. In recent years, molecular simulations have emerged as attractive tools for investigating the structure−selectivity relationship at a molecular level.[5−11] Simulating membrane separation processes generally requires utilizing techniques, such as non-equilibrium molecular dynamics (NEMD),[12] as such processes are almost always conducted under non-equilibrium conditions. While NEMD simulations have been extensively used for studying different aspects of driven transport across membranes, they are usually inefficient in accessing transport timescales that exceed $\sim 10^{-5}$ s. Probing, such timescales, has become possible only recently via combining NEMD with advanced sampling techniques. In particular, we recently employed[10] jumpy forward flux sampling (jFFS)[13] to accurately and efficiently probe arbitrarily long transport timescales for ions traversing a graphitic membrane with sub-nm nanopores.

Despite these advancements, molecular simulations of membrane separation are still at their infancy, and their sensitivity to system setup and other implementation details is yet to be fully investigated. One such overlooked aspect is *finite size effects*, that is, the extent to which transport kinetics and mechanism are affected by the size of the simulation box. Finite size effects are known to systematically impact estimates of thermodynamic,[14−21] structural[22] and transport[23−25] properties as well as rates of rare events such as nucleation.[26,27] While all such estimates eventually converge to their corresponding value in the thermodynamic limit upon increasing the system size, the rate of convergence tends to

Received: April 14, 2022
Published: November 3, 2022

be considerably slower for activated phenomena. Conducting a systematic analysis of finite size effects in membrane transport is critical because failing to do so might potentially lead to large errors in estimating solvent−solute and solute−solute selectivity as transport timescales of different chemical species might exhibit vastly different scalings with system size.

In this work, we use our previously developed approach based on jFFS[10] to probe the passage of chloride ions dissolved in aqueous NaCl solution through a sub-nm cylindrical pore etched within graphitic membranes of identical thicknesses and pore sizes but differing surface areas. We observe that ionic passage times have a strong dependence on a membrane cross-sectional area and change by as much as 6 orders of magnitude within the range of membrane areas considered here. Water flux, on the other hand, is virtually insensitive to the system size, which means that finite size effects result in the vast overestimation of selectivity and salt rejection rates. We confirm that such strong finite size effects are artifacts of periodic boundary conditions and are caused by the accumulation at the membrane surface of the surplus charge induced upon removing a chloride from the feed. Assuming that the feed is an ideal conductor, we develop a theory that correctly estimates the systematic error introduced as a result of periodicity and yields corrected generalized free energy profiles that match one another and exhibit no dependence on the system size. Our theoretical model provides a general framework that can be universally utilized to correct for finite size artifacts in simulations of ion transport through nanoporous membranes and biological channel proteins.

2. METHODS

2.1. System Setup and Relaxation.

The membranes considered in this work are comprised of three layers of graphite with sub-nm pores etched within them using the following procedure. In order to create a pore of the desired size, carbons are removed as needed from each full graphene sheet and hydrogens are attached to the carbons with missing bonds at a distance of 1.0919 Å along the lines connecting them to their now-missing neighbors. However, care must be taken in this approach in order to ensure that every carbon at the pore boundary only has one unpaired valence electron because hydrogen can only form a single bond. (This detail has been overlooked in several earlier works,[6,12] including our previous paper.[10]) We therefore propose a new method to assure the chemical fidelity of the constructed membranes. First, single and double bonds are drawn on a graphene sheet such that each carbon atom has one double bond and two single bonds (Figure 1A). A closed loop of the desired size is then identified so as to intersect single bonds only. The carbon atoms within the closed loop are then removed and the remaining carbons with missing neighbors become the binding sites for the passivating hydrogens (Figure 1B). It is necessary to note that in reality, double bonds are delocalized on a graphene sheet. There are, therefore, multiple ways of drawing the double bonds with each decoration leading to its own set of possible shapes and sizes.

After generating the passivated pore, the positions of hydrogen atoms are relaxed in a density functional theory (DFT) simulation using Gaussian 16[28] with the B3LYP functional[29] and an STO-3G basis set.[30] For the present membrane structure, the differences between initial and relaxed positions of the hydrogen atoms are negligible. The relaxed positions are then used to construct a three-layer graphite membrane perpendicular to the z axis. Graphene pistons are constructed using VMD[31] and are placed on either side of the membrane. Finally, PACKMOL[32] is used for adding sodium and chloride ions and water molecules to the feed and water molecules to the filtrate to generate 100 independent starting configurations. A representative configuration generated using this procedure is shown in Figure 1C. In order to examine the impact of system size on the kinetics of water and ion transport, this procedure is repeated to construct systems with identical ionic concentrations and pore geometries but with different box dimensions along the x and y directions. In particular, we examine systems with membrane cross-sectional areas of 12.53, 26.33, 32.60, 50.15, and 100.28 nm^2 in this work, with the corresponding box dimensions, the number of water molecules, and ion pairs given in Table 1.

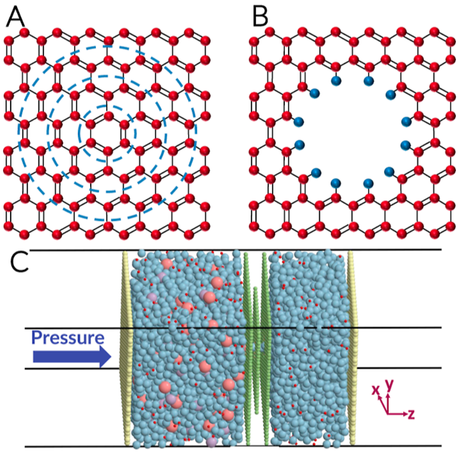

Figure 1. (A) Bond configuration giving rise to circular pores with single and double bonds drawn onto a graphene sheet and closed loops intersecting the single bonds only. (B) Removing the carbons within the loop interior and passivating the carbons with missing bonds with hydrogens yields the circular pore considered in this work. (C) Schematic representation of a filtration system comprised of three-layer graphitic membranes with a pore geometry and chemistry given in (B). Graphene pistons are placed at both ends to apply a pressure gradient of 196 atm. The feed and filtrate are filled with water molecules (light blue), sodium (light purple), and chloride (dark orange) ions as described in the text.

2.2. NEMD Simulations and System Equilibration.

Each independent starting configuration is equilibrated using LAMMPS,[33] an open source MD simulation engine. All atoms are represented as charged Lennard-Jones (LJ) particles, with water molecules and sodium and chloride ions modeled using the TIP3P[34] and Joung-Cheatham (JC)[35] force-fields,

Table 1. Summary of the Parameters Utilized for the System Setup, Including L_x and L_y, the Dimensions of the Simulation Box along the x and y Directions, $N_{w,feed}$ and $N_{w,filtrate}$, the Number of Water Molecules Added to the Feed and Filtrate Compartments, and $N_{i,feed}$, the Number of Ion Pairs Added to the Feed

L_x [nm]	L_y [nm]	area [nm^2]	$N_{w,feed}$	$N_{w,filtrate}$	$N_{i,feed}$
3.684	3.403	12.537	1616	1095	45
5.158	5.105	26.329	3393	2300	95
6.386	5.105	32.598	4220	2857	118
7.614	6.806	51.822	6473	4380	180
10.070	10.210	102.808	13,275	8982	371

respectively. The LJ parameters for carbons and passivating hydrogens were adopted from Müller-Plath[36] and Beu.[37] All interaction parameters, partial charges, and cutoff distances are given in our earlier publication.[10] All MD trajectories are carried out using the velocity-Verlet algorithm[38] while the temperature is maintained at 300 K using a Nosé-Hoover thermostat[39−41] with a damping time constant of 0.1 ps. The SHAKE algorithm[42] is used to maintain the rigidity of the water molecules. Long-range electrostatic interactions are estimated using the particle−particle−particle-mesh (PPPM) method[43] with a short-range cutoff of 1 nm. Periodic boundary conditions are only applied along the x and y directions in order to avoid artifacts due to unphysical long-range electrostatic interactions between the system and its periodic images along the z axis.[44] We therefore treat long-range interactions using a modified version of the PPPM method known as the slab PPPM.

Similar to our earlier works, we use an NEMD scheme in which the same force is exerted on all atoms within each piston in order to maintain a net pressure gradient of 196.6 bar across the membrane. For this purpose, we use the `fix aveforce` keyword in LAMMPS. During initial equilibration, the system is simulated for 10 ps with a time step of 0.5 fs while the pistons are kept fixed. We then allow the pistons to move according to the scheme described above and equilibrate the system for an additional 2 ns with a time step of 1 fs. The endpoints of these trajectories are utilized for the jFFS calculations described below wherein all trial trajectories are integrated using a time step of 1 fs.

2.3. Path Sampling Calculations. We compute ionic passage times using the forward-flux sampling[45] (FFS) method, an advanced path sampling technique that allows for efficient and accurate characterizations of rare events.[9] One of the main advantages of FFS is its ability to probe processes that occur in systems under external driving forces (such as pressure and concentration gradients) or with internally driven (e.g., self-propelling) building blocks (such as active matter systems). The temporal evolution of such systems does not generally obey detailed balance. As such, they cannot be studied using the advanced sampling techniques that involve backward integration of dynamic trajectories. FFS does not have this limitation. Therefore, in addition to being used for studying processes such as crystal nucleation,[46−56] hydrophobic evaporation,[57,58] and protein folding,[59] that generally occur in non-driven systems, it has been recently employed for probing internally driven processes such as phase separation[60] and morphological changes[61] in active matter systems, and externally driven processes such as protein rupture under a tensile force[62] and flow-induced polymer translocation,[63] and it is a remarkably powerful tool for probing the kinetics of pressure-driven ion transport. It must be emphasized that the corresponding rare events are almost always non-equilibrium and microscopically irreversible even if they occur in non-driven systems. Similar to other path sampling techniques, FFS requires constructing an order parameter, $\lambda(\cdot)$, a mechanical observable that is a measure of progress toward the completion of the rare event under consideration. In the case of ion passage through a rigid membrane, we choose $\lambda(\cdot)$ to be the curved-directed distance of the leading ion from the pore opening with larger λ values corresponding to a leading ion, which has traversed farther into the pore. The precise mathematical definition of $\lambda(\cdot)$ for our specific pore geometry is given in our earlier works.[10] In general, FFS characterizes the kinetics of transition between two (meta)stable basins that are demarcated by $\lambda(\cdot)$, that is, $A := \{x \in Q: \lambda(x) < \lambda_A\}$ and $B := \{x \in Q: \lambda(x) \geq \lambda_B\}$ and that are separated by large kinetic barriers. (Here, Q is the configuration space that contains all configurational degrees of freedom of the corresponding system.) In the case of membrane transport, these two basins are denoted by $F_{0,0}$ and $F_{0,1} \cup F_{1,0}$, where $F_{p,q}$ signifies the set of configurations in which p sodium and q chloride ions are present in the filtrate. While this OP does not distinguish between the sodium and chloride ions, the leading ion traversing the pore is always a chloride, due to the partial charge of the passivating hydrogens within the pore. Our approach, therefore, effectively probes the $F_{0,0} \to F_{0,1}$ transition consistent with our earlier work.[10]

Upon identifying a proper order parameter, an FFS calculation is initiated by sampling the starting basin (in this case, $F_{0,0}$) using unbiased NEMD trajectories launched from the independent configurations generated within A. After equilibration, a long NEMD trajectory is launched from each configuration and is monitored for first crossings of λ_0 every time it leaves A. The configurations corresponding to such crossings are saved for future iterations. Here, λ_0 ($>\lambda_A$) is a milestone sufficiently close to λ_A so that it can be reached frequently enough by trajectories initiated within A. These trajectories are terminated upon sufficient sampling of A, and the initial flux Φ_0, which corresponds to the number of first crossings of λ_0 per unit time, is estimated as

$$\Phi_0 := \frac{N_0}{T} \tag{1}$$

Here, N_0 is the total number of successful crossings of λ_0, while T is the total length of NEMD trajectories.

After finishing the sampling of the starting basin, another target milestone, λ_1, is specified. As outlined in our earlier publication,[13] λ_1 should be placed beyond $\lambda_{0,\max}$, or the largest value of the order parameter for configurations obtained after first crossing of λ_0. This procedure is in accordance with our newly developed jFFS algorithm,[13] since even though the OP employed here is not inherently jumpy, its discretization and the fact that it is computed every 0.5 ps leads to apparent jumps reported in our earlier work.[10] As such, obtaining accurate estimates of rate requires taking this apparent jumpiness into account. After setting λ_1, trial trajectories are then initiated from the stored configurations at or beyond λ_0, in which the velocities of water molecules and sodium and chloride ions are randomized according to the Boltzmann distribution. These trajectories are continued until they reach λ_1 or return to the starting basin. The configurations corresponding to the successful crossings of λ_1 are saved. After sufficient sampling, the transition probability from λ_0 to λ_1, $P(\lambda_1|\lambda_0)$, is computed by dividing the number of trajectories resulting in a successful crossing of λ_1 by the total number of trial trajectories. This process is repeated iteratively to compute transition probabilities between successive milestones. Once all the transition probabilities are known, the total rate is computed as

$$\Phi = \Phi_0 \prod_{k=0}^{N-1} P(\lambda_{k+1}|\lambda_k)$$

Note that τ, the mean first passage time for a trajectory initiated in A to reach B is then estimated as $\tau = 1/\Phi$.

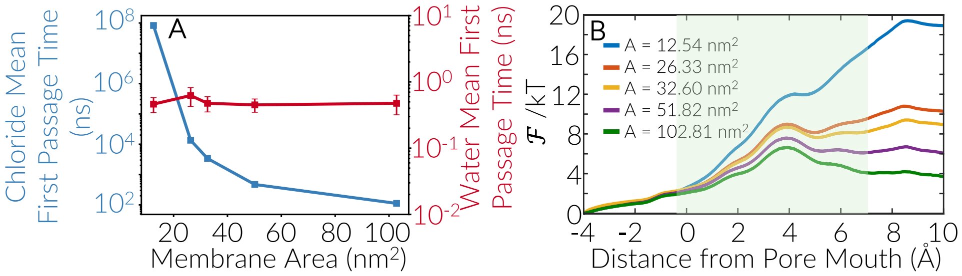

Figure 2. (A) Mean first passage time for chloride ions and water molecules and (B) generalized free energy profiles for different system sizes. The shaded region in (B) corresponds to the pore interior. System size impacts both the magnitude of the free energy barrier and the locus of the transition state.

2.4. Generalized Free Energy Profiles.

The notion of a Landau free energy $\mathcal{F}(\mathbf{q})$ over a collective variable space $\mathbf{q}$ can only be defined unambiguously for systems with stationary probability distributions.[9] Strictly speaking, this condition is not satisfied for non-equilibrium driven processes such as pressure-driven solute transport. However, one might still be able to define a generalized notion of free energy as long as the system is under pseudo-steady-state conditions. This is generally true for most non-equilibrium processes with long induction times. Here, we assume the existence of a notion of a generalized free energy, and compute it using the forward-flux sampling/mean first passage time (FFS-MFPT) method.[64] Considering the diffusive nature of the leading ion's motion, we can use the FFS-MFPT method only with minor adjustments to account for the apparent jumpiness in OP due to discretization and temporal coarse-graining. In particular, we estimate $\tau(\lambda;A)$, the mean first passage time for reaching $\lambda \in (\lambda_k,\lambda_{k+1}]$ from A, as

$$\tau(\lambda; A) = \frac{1}{M_k^{\lambda+}F_k^{\lambda+} + S_\lambda(1 - F_k^{\lambda+})} \{M_k^{\lambda+}\tau(\lambda_k; A) + (1 - F_k^{\lambda+})[L_\lambda^{(s)}S_\lambda + L_\lambda^{(f)}(M_k^{\lambda+} - S_\lambda)]\} \qquad (2)$$

Here, $F_k^{\lambda+}$ is the fraction of crossing events at λ_k that lands at a configuration with an order parameter value $\geq \lambda$, $M_k^{\lambda+}$ is the total number of trial trajectories during the $(k + 1)$th iteration launched from configurations with an order parameter value $< \lambda$, S_λ is the number of those trajectories that reach λ, and L_λ^{s} and L_λ^{f} are the average durations of the S_λ successful and $M_k^{\lambda+} - S_\lambda$ failing trajectories, respectively. The derivation of eq 2 is given in Appendix A.

3. RESULTS

Figure 2A depicts τ_{w} and τ_{c}, the mean first passage times for water molecules and chloride ions computed from conventional NEMD and jFFS calculations, respectively. While τ_{w} is virtually insensitive to the system size, τ_{c} exhibits a strong dependence on system size and varies by almost 6 orders of magnitude for the range of system sizes considered in this work. We also use the FFS-MFPT method to estimate $\mathcal{F}(\lambda)$, the generalized free energy profiles as a function of the order parameter, with the computed $\mathcal{F}(\lambda)$ profiles, as depicted in Figure 2B. Remarkably, the sensitivity of $\mathcal{F}(\lambda)$ to system size goes well beyond the magnitude of the free energy barrier and extends to the number and loci of the free energy maxima. More precisely, $\mathcal{F}(\lambda)$ exhibits two major peaks for smaller systems with the larger peak—and the main barrier to transport—located right after the pore exit. As the system size increases, however, the second peak weakens and eventually disappears. Therefore, the locus of the transition state moves discontinuously into the pore interior for sufficiently large system sizes. This dramatic change in the qualitative features of the translocation mechanism implies that examining a system that is too small will not only lead to an underestimation of the ionic flux but will also result in inaccurate identification of the ion transport mechanism.

In order to understand the origin of this strong sensitivity, we first compute $\langle -f_z \rangle$, the z component of the average restraining force exerted on the leading ion. As discussed in our earlier publication,[10] $\langle -f_z \rangle$ is non-vanishing even after the ion has left the pore, and its magnitude is determined by an interplay among ion-pore and ion−water interactions, the hydrodynamic resistance to ion mobility, and the charge anisotropy induced upon the passage of the leading ion. As can be seen in Figure 3A, there is no noticeable trend for the dependence of $\langle -f_z \rangle$ on system size. A clear trend emerges, however, upon decomposing $\langle -f_z \rangle$ into its ionic (Figure 3B) and non-ionic (Figure 3C) contributions. More precisely, $\langle -f_{z,\mathrm{ionic}} \rangle$, the force exerted on the leading ion by other ions in the system, is stronger in smaller systems and diminishes in magnitude upon increasing the system size. As discussed in detail in our earlier work,[10] $\langle -f_{z,\mathrm{ionic}} \rangle$ primarily arises due to the charge anisotropy induced by the leading ion within the feed. More precisely, when a chloride enters the pore, it induces a net charge surplus +e within the feed, which then exerts a restraining force on it. The observed differences in the ionic restraining force are, therefore, likely caused by how the distribution of the surplus charge is impacted by system size.

In order to determine how this excess charge is distributed within the feed, it is first necessary to characterize the intrinsic charge distribution within the feed prior to the leading chloride's entrance into the pore. This is achieved by partitioning the feed into cuboidal bins and computing the charge density within each bin. Considering the structuring of water molecules at the membrane surface, we demarcate the first few bins using the valleys of $\rho_{\mathrm{w}}(z)$, the water density as a function of z, and the distance from the membrane surface (Figure 4A). Within the plateau region of $\rho_{\mathrm{w}}(z)$, however, a uniform bin width of 0.5 nm is utilized. Figure 4B depicts the computed charge density profiles within $F_{0,0}$, that is, when all the ions are in the feed. Notably, a non-uniform charge distribution—a double layer in particular—is established at the membrane surface due to its overall affinity toward sodium ions. More precisely, the radially outward dipoles within the pore interior result in an affinity toward chlorides right at the

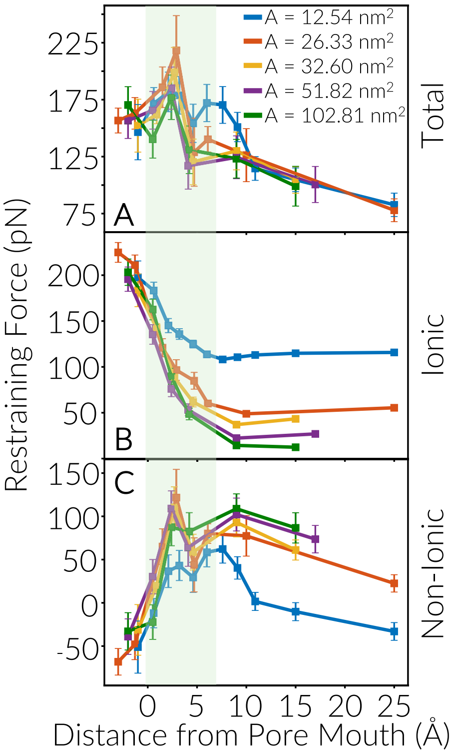

Figure 3. (A) $\langle -f_z \rangle$, the magnitude of the restraining force exerted on the leading ion at different FFS milestones as well as its breakdown to its (B) ionic and (C) non-ionic contributions.

pore entrance but sodium at the rest of the membrane surface. Considering the meager surface area of the pore opening in comparison to the rest of the membrane, the first layer of the liquid is populated by sodium ions overall, resulting in a positive charge density, followed by two layers dominated by chloride ions and a negative charge density. Note that these intrinsic profiles are independent of system size, suggesting that the strong sensitivity of rate and $\langle -f_{z,\text{ionic}} \rangle$ to system size is likely caused by the induced charges.

We then compute the induced charge density profiles by estimating the net charge profiles at different FFS milestones and subtracting from them the intrinsic profiles of Figure 4B. Figure 4C depicts the induced profiles for the smallest system. We observe that the induced charge resides entirely within the first two layers of water at the membrane surface. The accumulation of the excess charge at the membrane surface is qualitatively consistent with the feed compartment being an ideal conductor. From a physical perspective, this is a reasonable approximation because the sodium and chloride ions can act as mobile charge carriers that can redistribute until the average net electric field in the bulk vanishes.

The accumulation of excess charge at the membrane surface is observed for all system sizes (Figure S1). As can be seen in Figure 5A, the total induced charge is fully contained within the first two layers of water at the membrane surface irrespective of system size, which is the expected behavior if the feed acts as a conducting slab. Considering the larger surface area of the membrane in larger systems, this net excess charge is distributed over a larger area, which will lead to lower charge densities (Figure 5B) and likely smaller ionic restraining forces.

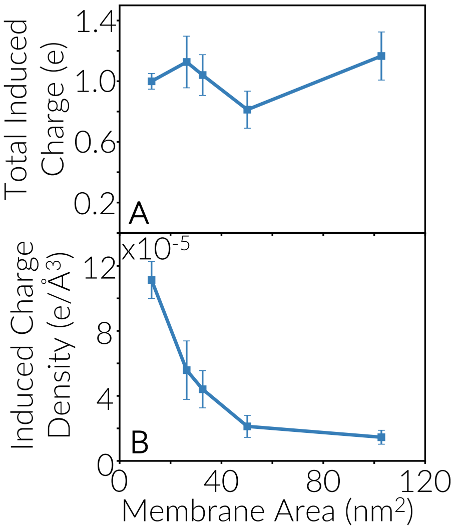

Figure 5. (A) Total induced charge and (B) induced charge density contained within the first two liquid layers at the membrane surface vs system size. Irrespective of system size, an induced charge of ≈+e is contained within the first two layers.

In order to determine whether our computed rates and generalized free energy profiles are quantitatively consistent with the feed compartment being an ideal conductor, we use the tools of electrostatics to calculate the lateral density of the

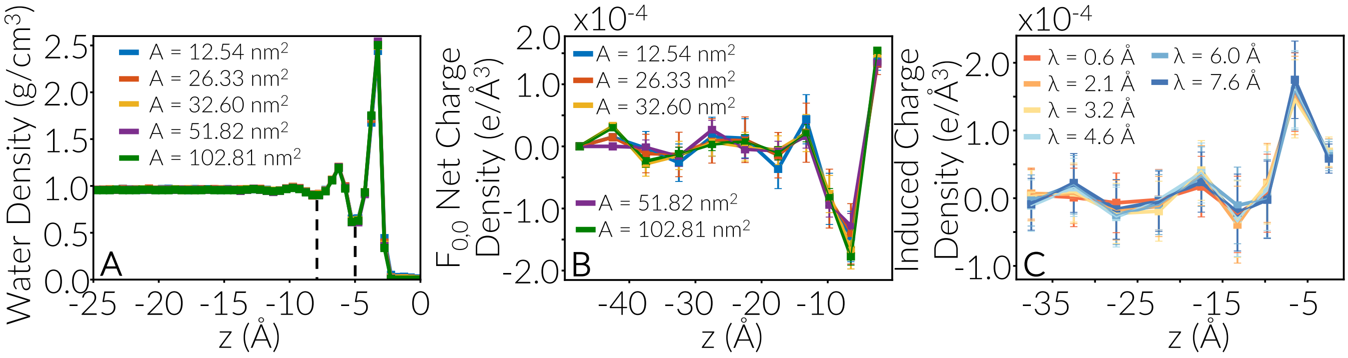

Figure 4. (A) Water and (B) net charge density within the feed compartment as a function of z, the distance from the membrane surface, in the $F_{0,0}$ basin, that is, before any charge anisotropy is established. Water density is computed using a cuboidal bins of thickness 0.25 Å while the binning scheme for the net charge density is discussed in the text. (C) Induced charge density in the system with the 12.53 nm^2 cross-sectional area, demonstrating that the induced charge is distributed in the first two liquid layers at the membrane surface.

accumulated excess charge, as well as the ensuing distortions in free energy. The charge density accumulated at the surface of an infinitely large conducting slab upon the removal of a monovalent anion from it can be estimated using the method of images and is given by

$$\rho_\infty(x, y) = \frac{eh}{2\pi[x^2 + y^2 + h^2]^{3/2}}. \tag{3}$$

Here, h is the distance of the anion from the surface of the slab. Note that $\rho_\infty(x,y)$ can be used for estimating the contribution of induced charge anisotropy to $\mathcal{F}(\lambda)$ in the thermodynamic limit. The observed dependence of τ_c and ΔF^* on system size, however, cannot be characterized using eq 3. This is because removing an anion from the feed compartment in a simulation box that is periodic along the x and y dimensions does result in the removal of all its periodic images, and each such periodic image will induce its own charge density within the slab. The ensuing total charge density accumulated at the membrane surface can be readily estimated using the superposition principle (see Appendix B), and $\tilde{\rho}_f(x, y) = L_x L_y \rho_f(x, y)/e$, the dimensionless charge density for the periodic system, will be given by

$$\tilde{\rho}_f(x, y) = 1 + 2\sum_{\alpha\in\{x,y\}}\sum_{k_\alpha=1}^{+\infty} e^{-q_\alpha h}\cos q_\alpha \alpha + 2\sum_{k_x,k_y=1}^{+\infty} e^{-|\mathbf{q}|h}\sum_{p=\pm1}\cos(q_x x + p q_y y) \tag{4}$$

wherein $\mathbf{q} = (2\pi k_x/L_x, 2\pi k_y/L_y) \in \mathbb{R}^2$ is the wavevector associated with $(k_x, k_y) \in \mathbb{N}^2$. While we cannot directly test the validity of eq 4 due to a lack of sufficient statistics, we can use eq 4 to determine the excess increase in $\mathcal{F}(\lambda)$ due to $\Delta\rho(x,y) = \rho_f(x,y) - \rho_\infty(x,y)$. This is achieved by estimating the excess electric field induced by $\Delta\rho(x,y)$ and integrating it to obtain the following correction to the free energy

$$\frac{\Delta\mathcal{F}_{corr}(z)}{kT} = \frac{e^2}{2\epsilon_0 kTL_xL_y}\left\{z - z_0 - \frac{L_xL_y}{2\pi}\left[\frac{1}{z_0 + z} - \frac{1}{2z_0}\right] - 2\sum_{\alpha\in\{x,y\}}\sum_{k_\alpha=1}^{+\infty}\frac{e^{-2q_\alpha z} - e^{-q_\alpha(z+z_0)}}{q_\alpha} - 4\sum_{k_x,k_y=1}^{+\infty}\frac{e^{-2|\mathbf{q}|z} - e^{-|\mathbf{q}|(z+z_0)}}{|\mathbf{q}|}\right\} \tag{5}$$

Here, ϵ_0 and k are the vacuum permittivity and the Boltzmann constant, respectively, and z_0 is the distance from the conductor surface at which the anion is fully detached from the feed and the induced charge density is established. It is not trivial to rigorously define what constitutes "full detachment" considering the connectivity of the leading ion to the feed through a train of water molecules. One can, however, argue that the leading chloride becomes fully detached when its first hydration shell has completely left the first liquid layer at the membrane surface. This will correspond to $\lambda \approx 0$, that is, when the ion starts entering the pore. This assertion is corroborated by our observation that the $\mathcal{F}(\lambda)$ profiles start diverging at $\lambda \approx 0$, as can be seen in Figure 2B.

Prior to applying this correction to the free energy profiles, as depicted in Figure 2B, two additional points need to be addressed. First, the free energy correction given in eq 5 is a function of z, which differs from the curvilinear order parameter utilized in FFS and only aligns with it within the pore interior. Because the size-dependent uphill portion of $\mathcal{F}(\lambda)$ is mostly contained within the pore interior, any errors due to such mismatch will be minimal (and likely inconsequential). The second issue is that both z and z_0 correspond to the distance from the surface of the conductor which does not necessarily coincide with the membrane surface. While such a distinction might be unimportant at the macroscopic scale, it can become significant at a molecular level. Moreover, the region in which the induced excess charge is distributed will be diffuse, which will make it nontrivial to define what constitutes the conductor surface. Considering our observation that the excess charge is almost fully contained within the first two layers of water at the immediate vicinity of the membrane, we define z_c, the locus of the conductor surface, as the geometric center of the induced charges within the first two liquid layers. More precisely, we compute z_c as $z_c = (z_1q_{i,1} + z_2q_{i,2})/(q_{i,1} + q_{i,2})$ wherein z_j and $q_{i,j}$ are the average z coordinate of and the total induced charge contained within the jth liquid layer, respectively. Using this definitions, we obtain z_c values that are for the most part independent of the system size and vary between −0.46 and −0.41 nm as can be seen in Table 2.

Table 2. Location of the Surface of the Feed Conductor, z_c, in the Ideal Conductor Model[a]

area [nm^2]	z_c [nm]
12.537	−0.464 ± 0.014
26.329	−0.430 ± 0.054
32.598	−0.443 ± 0.044
51.822	−0.421 ± 0.046
102.808	−0.412 ± 0.040

[a] All uncertainties correspond to 95% confidence intervals.

After estimating the model parameters, we subtract the finite size correction given by eq 5 from $\mathcal{F}(\lambda)$ profiles, as depicted in Figure 2B to compute $\mathcal{F}_\infty(\lambda) \equiv \mathcal{F}_f(\lambda) - \mathcal{F}_{\text{corr}}(\lambda)$, the generalized free energy profile in the thermodynamic limit. The corrected free energy profiles are depicted in Figure 6A. While each profile has been estimated independently, that is, only using the information obtained from the corresponding finite size simulation, they are all in excellent agreement with one another both in terms of the loci of the transition state and the magnitudes of the free energy barrier. Overall, they predict a transition state that is located at $\lambda^* \approx 0.38 \pm 0.02$ nm and has a free energy barrier of $\Delta\mathcal{F}_\infty(\lambda^*)/kT = 6.82 \pm 0.12$. The barriers obtained from the individual profiles are also fairly consistent and vary between 6.1kT and 7.2kT. This is in stark contrast to the original (uncorrected) free energy profiles that exhibit substantial differences not only in terms of the locus of the transition state but also the magnitude of the free energy barrier, the latter varying by 13kT.

The next step is to estimate τ_c in the thermodynamic limit. While it is in principle possible to relate the free energy profile to the passage time using the reaction rate theory,[65] doing so requires estimating $D(\lambda)$, or diffusivity along the $\mathcal{F}_f(\lambda)$ and $\mathcal{F}_\infty(\lambda)$ free energy landscapes. For sufficiently large free energy

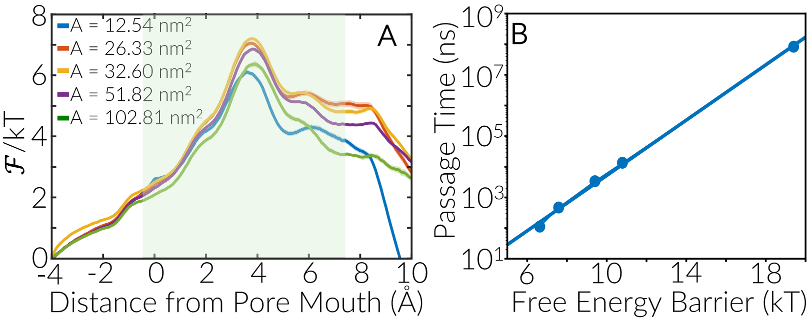

Figure 6. (A) Corrected generalized free energy profiles for different system sizes after applying the ideal conductor model. (B) Linear relationship between $\Delta\mathcal{F}_f^*$ and ln $\tau_{c,f}$.

Table 3. Estimates of τ_c and $\Delta\mathcal{F}^*/kT$ from jFFS and Extrapolations to the Thermodynamic Limit Using the Ideal Conductor Model[a]

L_x [nm]	L_y [nm]	area [nm^2]	$\tau_{c,f}$ [ns]	$\Delta\mathcal{F}_f^*/kT$	$\Delta\mathcal{F}_\infty^*/kT$	$\tau_{c,\infty}$ [ns]
3.684	3.403	12.537	$(8.29 \pm 0.53) \times 10^7$	19.40 ± 0.10	6.11 ± 0.12	140 ± 48
5.158	5.105	26.329	$(1.36 \pm 0.17) \times 10^4$	10.79 ± 0.06	7.05 ± 0.14	322 ± 117
6.386	5.105	32.598	$(3.38 \pm 0.17) \times 10^3$	9.41 ± 0.04	7.20 ± 0.14	372 ± 79
7.614	6.806	51.822	$(4.69 \pm 0.58) \times 10^2$	7.58 ± 0.08	6.86 ± 0.10	228 ± 68
10.070	10.210	102.808	$(1.12 \pm 0.16) \times 10^2$	6.63 ± 0.22	6.37 ± 0.22	86 ± 64

[a] All uncertainties correspond to 95% confidence intervals.

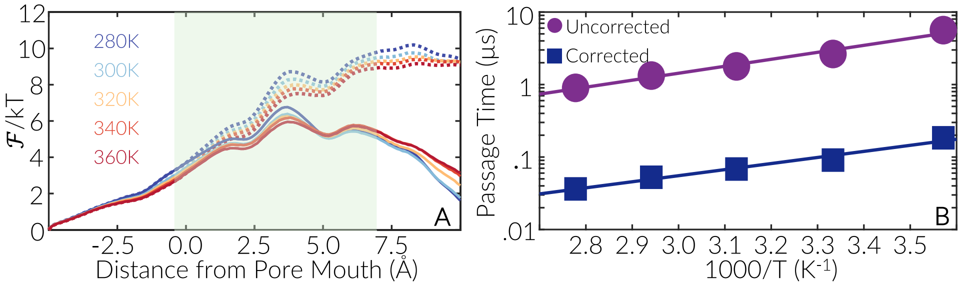

Figure 7. (A) $\mathcal{F}_f(\lambda)$ (dashed) and $\mathcal{F}_f(\lambda)$ (solid) profiles computed for the membrane considered in ref 10. (B) Arrhenius plots for the original (dark purple) and corrected (dark blue) τ_c values.

barriers, however, it can be demonstrated that the passage time will be given by $\tau = \mathcal{A}\exp[+\Delta\mathcal{F}^*/kT]$, wherein $\mathcal{A}$ is a prefactor that depends on, among other things, the local curvatures of the starting basin and the transition state.[66,67] Intuitively, this expression is based on the assumption that a quasi-equilibrium is established between the starting basin and the transition state. We argue that $\mathcal{A}$ has to be insensitive to system size. This assertion is motivated by the observed mechanism of finite size scaling that kicks in when the ion fully enters the pore and is bolstered by the insensitivity of properties such as τ_w and the pre-entrance portion of $\mathcal{F}(\lambda)$ to system size. Moreover, the validity of this assertion is unambiguously corroborated by the perfect linear scaling between ln τ_c and $\Delta\mathcal{F}^*$ ($R^2 = 0.99$), as depicted in Figure 6B. It is therefore reasonable to argue that $\tau_{c,\infty}$ can be estimated as

$$\tau_{c,\infty} = \tau_{c,f}\exp\left[\frac{\Delta\mathcal{F}_\infty^* - \Delta\mathcal{F}_f^*}{kT}\right] \tag{6}$$

Equation 6 can be used to estimate τ_c in the thermodynamic limit from the information obtained from each simulation, with the corresponding estimates, as given in Table 3. While these $\tau_{c,\infty}$'s have been estimated independently, they only differ by a factor of four despite the astronomical differences among the τ_c's computed for finite systems. A holistic estimate can, however, be obtained by using the linear correlation, as depicted in Figure 6B. More precisely, a $\Delta\mathcal{F}_\infty^*/kT = 6.82 \pm 0.12$ yields a passage time of $\log_{10} \tau_{c,\infty}$ [ns] = 2.35 ± 0.45 (or $\tau_{c,\infty} = 224^{+407}_{-144}$ ns), which is consistent with the individual estimates given in Table 3.

We finally examine the sensitivity of the conclusions from our earlier works[10] to the finite size effects discussed here. While the box dimensions in ref 10 match those of the second smallest system in this work, the pore chemistries are slightly different, as discussed in Section II A. Such differences not only affect the kinetics and mechanisms of ion transport but also impact the sensitivity to finite size effects. The latter is due to the fact that the geometric spread of the accumulated induced charge is impacted by the chemistry of the membrane surface and the pore entrance. Comparing the passage times and free energy barriers computed for both systems reveals that the ion transport appears to be more restricted for the pore chemistry considered here, resulting in an increase in τ_c from 2.64 ± 0.16 μs in ref 10 to 13.6 ± 1.7 μs here. Applying the ideal conductor model, however, leads to $\tau_{c,\infty}$ values that are almost statistically indistinguishable (126 ± 36 ns for ref 10 vs 322 ± 117 ns for

https://doi.org/10.1021/acs.jctc.2c00375
J. Chem. Theory Comput. 2022, 18, 7142−7154

the current work). This is a vivid demonstration of the fact that the magnitude of the finite size correction to the generalized free energy profile can be system-dependent due to the sensitivity of z_c to the membrane and pore chemistry.

Figure 7A depicts the original and corrected free energy profiles for the system considered in ref 10. Unlike the pore chemistry considered in this work, the dominant free energy peak observed in finite-size simulations does not fully disappear in the thermodynamic limit and only becomes less dominant in comparison to the peak at the middle of the pore. It is also noteworthy that the $\tau_{c,\infty}$'s estimated at different temperatures exhibit an Arrhenius dependence on T with an activation barrier of $\Delta E_{c,\infty} = 16.0 \pm 4.7$ kJ/mol. Note that $\Delta E_{c,\infty}$ is slightly smaller than $\Delta E_{c,f} = 18.4 \pm 4.4$ kJ/mol (Figure 7B) but is still larger than the activation barrier for water transport.

4. DISCUSSION AND CONCLUSIONS

This work constitutes the first systematic investigation of how the size of the simulation box will impact the timescales of water and ion transport through semipermeable nanoporous membranes under non-equilibrium and driven conditions. Similar to our earlier works,[10] we use a thin graphite-based membrane with a sub-nm cylindrical pore as a test case and vary the lateral dimensions of the membrane while keeping the pore size and chemistry and the compartment concentrations fixed. By using NEMD and jFFS, we compute the mean first passage times for water molecules and chloride ions as a function of the system size. While water fluxes are virtually insensitive to system size, ionic transport timescales vary by almost 6 orders of magnitude and decrease as the system size increases. Our examination of generalized free energy barriers (estimated from the FFS-MFPT method) points not only to a wide $13kT$ spread in the free energy barrier but also to a qualitative change in the perceived mechanism of transport. For smaller systems, $\mathcal{F}(\lambda)$ exhibits two major peaks, with the higher one located right outside the pore exit. As the system size increases, however, the second peak weakens and eventually disappears. As a result, the locus of the main barrier moves discontinuously from outside the pore exit to the middle of the pore.

By carefully examining the force exerted on the leading ion, we attribute these intriguing observations to the differential distribution on the membrane surface of the surplus charge induced within the feed compartment as a result of the leading ion's entrance into the pore. To better quantify the observed finite size artifacts, we develop a theoretical model assuming that the feed compartment is an ideal conductor. Despite the stark quantitative and qualitative differences between the generalized free energy profiles computed for different system sizes, subtracting the correction term predicted by our theoretical model yields free energy profiles that collapse onto one another and become statistically indistinguishable. Our physics-based approach therefore constitutes a blueprint for rigorously removing finite-size artifacts from the fluxes and free energy profiles obtained from computational studies of hindered ion transport.

It must be emphasized that the scaling of activation barriers and ionic passage times with system size does not only depend on the dimensions of the simulation box but is also likely to be impacted by other features, such as the size, arrangement, and chemistry of the pores. When it comes to our ideal conductor theory, these structural features impact the thickness and location of what constitutes the surface of the ideal conductor and henceforth, the z_c parameter. Therefore, comparing the passage times and free energy barriers of two or more finite systems with identical box dimensions but different pore chemistries and arrangements without applying finite size corrections can be perilous and might lead to incorrect and misleading conclusions. This can be vividly observed in comparing the two otherwise identical pores that only have slightly different passivation patterns, namely, the pores considered in our earlier works[10] and those considered here. While ion transport appears to be almost an order of magnitude faster through the former, the two membranes tend to have almost identical free energy barriers and passage times in the thermodynamic limit. This is therefore an important point that needs to be taken into account in studies that involve probing a design parameter space.

Apart from their importance in making molecular simulations of ionic transport through membranes more accurate, our findings might shed some light onto apparent discrepancies between experimental and computational studies of ion transport, for example, in water desalination. While most computational studies report salt rejection rates of 100%,[5−8] experimental studies generally yield smaller rejection rates.[68−72] Part of this disagreement is due to defects in real membranes,[73] but our work suggests that the finite sizes of the simulation boxes considered in simulation studies might also lead to a massive overestimation of ionic passage times and salt rejection rates. Considering the linear scaling of $\Delta\mathcal{F}_{corr}$ with z as $z \to \infty$, such discrepancies are expected to be larger for thicker membranes.

While estimating the precise correction term to be subtracted from $\mathcal{F}(\lambda)$ requires applying the full ideal conductor model, a conservative upper bound can still be obtained from the dimensions of the membrane and its dielectric constant. More specifically, assuming the worst case scenario in which the transition state is located right at the membrane exit (i.e., on the filtrate side), and that the excess charge is almost uniformly distributed at the membrane surface, $\Delta\mathcal{F}^*_{\text{corr}}$, the correction term at the top of the activation barrier will be bounded from above by

$$\frac{\Delta\mathcal{F}^*_{corr}}{kT} \leq \underbrace{\frac{Z^2 e^2}{2\epsilon_0 kT}}_{\alpha} \underbrace{\frac{l_m}{L_x L_y \langle\epsilon_r\rangle}}_{\kappa} \tag{7}$$

where Z is the valence of the traversing ion and l_m is the thickness of the membrane. Note that α only depends on the temperature, while κ is a function of the dimensions of the membrane as well as the normal component of its dielectric constant tensor. Therefore, eq 7 can be used as a heuristic to a priori choose L_x and L_y so that $\Delta\mathcal{F}^*_{corr}$ is smaller than an acceptable threshold, for example, a few kT's.

The framework proposed here can, in principle, be applied to the problem of sodium transport, that is, to the $F_{0,1} \to F_{1,1}$ transition in which the first sodium traverses the pore after a chloride has already reached the filtrate. Qualitatively, one would expect the sodium passage time to increase dramatically as the system size increases because the leading sodium will be under an excess electrostatic "pull-forward" force even at $F_{0,1}$, that is, while still inside the feed compartment. Therefore, the $F_{0,1}$ basin will be further destabilized in comparison to the top of the barrier. There are, however, several outstanding technical obstacles to quantifying this effect. First of all, the destabilization of the $F_{0,1}$ implies that a curvature correction needs to be applied to resolve the mismatch between the curved directed distance from the pore entrance and the perpendicular distance from the membrane surface. The more daunting challenge, however, is the need to estimate $\epsilon_r(z)$, the z-dependence normal component of the dielectric constant tensor at the immediate vicinity of the membrane surface. As has been demonstrated before, dielectric constants change drastically upon confinement. In the case of water, for instance, the dielectric constant can change by over an order of magnitude with respect to the bulk.[74,75] Moreover, as discussed elsewhere, it is not straightforward to calculate anisotropic and position-dependent dielectric constants, as the existing methodologies can also exhibit strong finite size effects even when dealing with an insulating medium, such as pristine water.[76] Exploring these technical challenges and developing robust algorithms for estimating position-dependent dielectric constants is necessary for correcting the passage times and generalized free energy profiles for the $F_{0,1} \to F_{1,1}$ transition. Addressing these challenges is beyond the scope of this work and they will be topics of follow-up studies.

One of the key underlying assumptions of the ideal conductor model is that charge carriers within the conductor are infinitesimally small. This condition, however, is not satisfied in molecular simulation wherein a finite number of charge carriers are present. This non-ideality appears to have no noticeable impact on the performance of the ideal conductor model here. This might, however, no longer be the case in situations in which the excess or deficit charge is carried by a small number of charge carriers. For instance, such non-ideality can have profound impacts on correcting for finite size effects in the $F_{0,1} \to F_{1,1}$ transition wherein the deficit charge in the filtrate is only carried by a single ion. Further follow-up studies are needed for determining the conditions under which the small number of charge carriers might impact the predictive power of the ideal conductor model.

Another key assumption of the ideal conductor model is that charge carriers can reorganize instantaneously in response to electrostatic perturbations. In real systems, however, there is always a characteristic timescale for the diffusion of charge carriers, resulting in a lag between the stimulus (the motion of the leading ion) and the response (charge rearrangement at the membrane surface). A reasonable proxy for such a lag is the cage escape time, which can be evaluated as $\tau_{\text{cage}} = l_r^2/D$ where l_r and D are the locus of the first valley of the radial distribution function and the diffusivity, respectively. We use the Einstein relationship to compute the ionic diffusivities from mean-squared displacements (Figure S2). Using the computed diffusivities ($D_{\text{chloride}} = 1.40 \times 10^{-9}$ m^2·s^{-1} and $D_{\text{sodium}} = 1.98 \times 10^{-9}$ m^2·s^{-1}) and the loci of the first valleys of RDF obtained in ref 10 ($l_{r,\text{sodium}} = 0.325$ nm and $l_{r,\text{chloride}} = 0.375$ nm), we estimate the cage escape times to be 75 and 71 ps for sodium and chloride, respectively. These are both comparable in magnitude to the typical length of a trial FFS trajectory (a few tens of picoseconds). This implies that the lag between the stimulus and the response is negligible here. Such a lag, however, might become significant when the feed is viscous or when charge carriers are bulkier and have considerably smaller diffusivities. The latter can, for instance, happen in solutions of charged polymers or biomolecules. Another situation that might make such lags important is when a system experiences oscillatory electric fields. Determining a charge carrier diffusivity below which such lags become important is beyond the scope of this work and will be the topic of future studies.

It is important to note another limitation of our approach in dealing with graphite- and graphene-based membranes. While the force-field employed in this work represents graphite as rigid and non-polarizable, real graphite is an electrical conductor. An NEMD simulation carried out using a more sophisticated approach that takes graphite's conductivity into account is expected to be less susceptible to the type of finite size artifacts reported here. This is because the induced charges accumulated at the membrane surface will create additional image charges within the conducting membrane, which will weaken their impact on the leading ion. It must be emphasized that finite size effects will still be present because the pore interior will not be conducting. Correcting for such artifacts, however, will require a more sophisticated approach and is beyond the scope of this work.

It must also be noted that our model is a powerful framework for studying the transport of ions and charge macromolecules through biological membranes and channel proteins. It has indeed been demonstrated that ion transport through channel proteins will be significantly slower when non-polarizable force-fields are utilized.[77] While such apparent slowdown could be partly caused by the limitations of non-polarizable force-fields, they might also arise from the types of finite size effects discussed in this work. Therefore, even though polarizable force-fields might be less susceptible to such artifacts, equally accurate estimates of passage times might still be attainable from non-polarizable models if finite size effects are properly corrected.

■ APPENDIX A

Derivation of Eq 2

In order to prove eq 2, we use notations similar to the ones introduced in our earlier paper.[13] In particular, for a discrete-time NEMD trajectory $X \equiv (x_0, x_1, x_2, ...)$, we reuse the following random variables and functions already introduced in ref 13

$$L[X] = \min_{q>0}\{x_q \notin A\} \tag{A1}$$

$$T_B[X] = \min_{q \geq L[X]}\{x_q \in A \cup B\} \tag{A2}$$

$$W_B[X] = \Theta_B(x_{T_B[X]}) \tag{A3}$$

$$T_i[X] = \min_{q \geq L[X]}\{x_q \notin \cup_{j=0}^{i} C_{j-1}\} \tag{A4}$$

$$W_i[X] = \theta_i(x_{T_i[X]}) \tag{A5}$$

$$U_{i,j}[X] = \begin{cases} \theta_i(x_{T_i[X]})\theta_j(x_{T_{i+1}[X]}) & i \geq 0 \\ \phi_0(x_{L[X]})\theta_j(x_{T_0[X]}) & i = -1 \end{cases} \tag{A6}$$

$$\phi_i(x) = \sum_{j=0}^{i} \theta_{j-1}(x) \tag{A7}$$

Here, $C_i = \{x_Q\colon \lambda_i \leq \lambda(x) < \lambda_{i+1}\}$, while $\theta_B(x)$ and $\theta_i(x)$ are the indicator functions for B and C_i, respectively. Moreover, for any $\lambda_k < \lambda \leq \lambda_{k+1}$, we define the following random variables

$$T_\lambda[X] = \min_{q \geq L[X]}\{\lambda(x_q) \geq \lambda, \text{ or } x_q \in A\} \tag{A8}$$

https://doi.org/10.1021/acs.jctc.2c00375
J. Chem. Theory Comput. 2022, 18, 7142−7154

$$W_\lambda[X] = \begin{cases} 1 & \lambda(x_{T_\lambda[X]}) \geq \lambda \\ 0 & x_{T_\lambda[X]} \in A \end{cases} \tag{A9}$$

$$U_{k-1,\lambda}[X] = \begin{cases} 1 & \lambda(x_{T_k[X]}) \geq \lambda \\ 0 & \text{otherwise} \end{cases} \tag{A10}$$

For simplicity, we assume that FFS milestones are placed so that the simplified variant of jFFS introduced in ref 13 can be employed, that is, that no multi-milestone jumps are observed. This will imply that $U_{i,j}$ will always be zero for $j > i + 1$. This assumption considerably simplifies the procedure for computing $\langle T_\lambda\rangle$ and $\langle W_\lambda\rangle$, which are both needed for estimating the $\tau(\lambda;A)$ given in eq 2. In particular, $\langle T_\lambda\rangle$ can be estimated as

$$\begin{aligned}\langle T_\lambda\rangle_{\mathcal{E}_A} &= \langle T_k\rangle_{\mathcal{E}_A} + \langle T_\lambda - T_k | U_{k-1,\lambda} = 1\rangle_{\mathcal{E}_A} P(U_{k-1,\lambda} = 1) \\ &\quad + \langle T_\lambda - T_k | U_{k-1,\lambda} = 0\rangle_{\mathcal{E}_A} P(U_{k-1,\lambda} = 0) \\ &\overset{(a)}{=} \langle T_k\rangle_{\mathcal{E}_A} \\ &\quad + \langle T_\lambda - T_k | W_\lambda = 1, U_{k-1,\lambda} = 0, \mathbf{U}_k = \mathbf{1}\rangle_{\mathcal{E}_A} \\ &\quad \times P(W_\lambda = 1, U_{k-1,\lambda} = 0, \mathbf{U}_k = \mathbf{1}) \\ &\quad + \langle T_\lambda - T_k | W_\lambda = 0, U_{k-1,\lambda} = 0, \mathbf{U}_k = \mathbf{1}\rangle_{\mathcal{E}_A} \\ &\quad \times P(W_\lambda = 0, U_{k-1,\lambda} = 0, \mathbf{U}_k = \mathbf{1}) \\ &= \langle T_k\rangle_{\mathcal{E}_A} + P(\mathbf{U}_k = \mathbf{1}) \times (1 - F_k^{\lambda+}) \\ &\quad \left[L_\lambda^{(s)} \frac{S_\lambda}{M_k^{\lambda+}} + L_\lambda^{(f)} \frac{M_k^{\lambda+} - S_\lambda}{M_k^{\lambda+}}\right]\end{aligned} \tag{A11}$$

Here, $\mathbf{U}_k \equiv= (U_{-1,0}, U_{0,1}, U_{1,2}, ..., U_{k-1,k})$, 1 is a $(k + 1)$-dimensional vector of ones, $\mathcal{E}_A$ is the space of all trajectories initiated from A, $F_k^{\lambda+}$ is the fraction of crossing events at λ_k that land at a value $\geq\lambda$, $M_k^{\lambda+}$ is the number of trial trajectories initiated from the configurations landed before λ, and S_λ is the number of those that reach λ. $L_\lambda^{(s)}$ and $L_\lambda^{(f)}$ correspond to the average length of successful and failing trajectories (computed for the $M_k^{\lambda+}$ trajectories launched from configurations prior to λ), respectively, wherein success corresponds to reaching λ. Note that (a) follows from the fact that $T_k[X] = T_\lambda[X]$ when $U_{k-1,\lambda}[X] = 1$ or $\mathbf{U}_k \neq 1$. Similarly, $P(W_\lambda = 1)$ can be estimated as

$$\begin{aligned}P(W_\lambda = 1) &= P(W_\lambda = 1, \mathbf{U}_k = \mathbf{1}) \\ &= \sum_{b=0}^{1} P(W_\lambda = 1, \mathbf{U}_k = \mathbf{1}, U_{k-1,\lambda} = b) \\ &= \sum_{b=0}^{1} P(W_\lambda = 1 | U_{k-1,\lambda} = b, \mathbf{U}_k = \mathbf{1}) \\ &\qquad \times P(U_{k-1,\lambda} = b | \mathbf{U}_k = \mathbf{1}) P(\mathbf{U}_k = \mathbf{1}) \\ &= \left[\frac{S_\lambda}{M_k^{\lambda+}}(1 - F_k^{\lambda+}) + 1 \cdot F_k^{\lambda+}\right] P(\mathbf{U}_k = \mathbf{1})\end{aligned} \tag{A12}$$

Equation 2 can then be derived from eqs A11 and A1A12 by noting that $\tau(\lambda; A) = \langle T_\lambda\rangle_{\mathcal{E}_A} / \langle W_\lambda\rangle_{\mathcal{E}_A}$.

APPENDIX B

Derivation of Eqs 4 and 5

Supposing that a monovalent anion is removed from an ideal conducting slab that is infinitely large in the x and y dimensions and that has its top surface at $z = 0$. Assuming that the anion is located at $(0, 0, h)$, the charge density induced by its removal can be readily estimated from the method of images and is given by eq 3. Now suppose that the anion is removed from a finite ideal conductor (with lateral dimensions L_x and L_y) that is also periodic along the x and y dimensions. Under such a scenario, all the periodic images of that ion will also leave the conductor simultaneously, and the resulting induced charge density can be estimated from the superposition principle

$$\begin{aligned}\rho_f(x, y) &= \frac{eh}{2\pi} \sum_{k_x, k_y = -\infty}^{+\infty} \frac{1}{[(x - k_x L_x)^2 + (y - k_y L_y)^2 + h^2]^{3/2}} \\ &= \sum_{k_x, k_y \in \mathbb{Z}} \rho_\infty(x - k_x L_x, y - k_y L_y)\end{aligned} \tag{B1}$$

It must be noted that $\rho_f(x,y)$ is periodic along the x and y directions and can thus be expressed as the following Fourier series

$$\rho_f(x, y) = \frac{1}{L_x L_y} \sum_{k_x, k_y} e^{i(q_x x + q_y y)} \times \underbrace{\int_0^{L_x} \int_0^{L_y} e^{-i(q_x \xi + q_y \eta)} \rho_f(\xi, \eta)\, d\xi\, d\eta}_{a_{k_x, k_y}} \tag{B2}$$

Note that $\mathbf{q} = (2\pi k_x / L_x, 2\pi k_y / L_y) \in \mathbb{R}^2$ is the wavevector associated with $(k_x, k_y) \in \mathbb{Z}^2$. The goal is to use the symmetries of $\rho_\infty(x,y)$ and $\rho_f(x,y)$ to estimate a_{k_x,k_y} and to express $\rho_f(x,y)$ in the reciprocal space. By combining eqs B1 and BB2, it can be demonstrated that

$$\begin{aligned}a_{k_x,k_y} &= \sum_{j_x, j_y \in \mathbb{Z}} \int_0^{L_x} \int_0^{L_y} e^{-i(q_x \xi + q_y \eta)} \\ &\quad \times \rho_\infty(\xi - j_x L_x, \eta - j_y L_y)\, d\xi\, d\eta \\ &= \sum_{j_x, j_y \in \mathbb{Z}} \int_{-j_x L_x}^{(1 - j_x) L_x} \int_{-j_y L_y}^{(1 - j_y) L_y} e^{-i(q_x \bar{\xi} + q_y \bar{\eta})} \times \rho_\infty(\bar{\xi}, \bar{\eta}) \\ &\quad d\bar{\xi}\, d\bar{\eta} \\ &= \int_{-\infty}^{+\infty} \int_{-\infty}^{+\infty} e^{-i(q_x \bar{\xi} + q_y \bar{\eta})} \rho_\infty(\bar{\xi}, \bar{\eta})\, d\bar{\xi}\, d\bar{\eta} \\ &= \widehat{\rho_\infty}\left(\frac{\mathbf{q}}{2\pi}\right)\end{aligned} \tag{B3}$$

Here, $\widehat{\rho_\infty}(\cdot)$ is the Fourier transform of $\rho_f(\cdot)$, which can be readily calculated by noting that $\rho_\infty(x,y)$ is a radial function, that is, that $\rho_\infty(x, y) = f(\sqrt{x^2 + y^2})$. Therefore, according to the scaling theorem for Fourier transforms,[79] $\widehat{\rho_\infty}(q_x/2\pi, q_y/2\pi)$ will also be a radial function in the reciprocal space, that is, it will only depend on $|\mathbf{q}| = \sqrt{q_x^2 + q_y^2}$. As such, for any $\mathbf{q} = (q_x, q_y)$, it suffices to estimate $\widehat{\rho_\infty}(\mathbf{q})$ for $(|\mathbf{q}|,0)$. $\widehat{\rho_\infty}(\mathbf{q})$ will thus be given by

$$\begin{aligned}\widehat{\rho_\infty}\left(\frac{\mathbf{q}}{2\pi}\right) &= \frac{\mathrm{e}h}{2\pi}\int_{-\infty}^{+\infty}\int_{-\infty}^{+\infty}\frac{e^{-i|\mathbf{q}|\xi}}{[\xi^2+\eta^2+h^2]^{3/2}}\,\mathrm{d}\eta\,\mathrm{d}\xi \\ &= \frac{\mathrm{e}h}{\pi}\int_{-\infty}^{+\infty}\frac{\mathrm{e}^{-i|\mathbf{q}|\xi}}{\xi^2+h^2}\,\mathrm{d}\xi \overset{\text{(a)}}{=} \mathcal{E}\mathrm{e}^{-|\mathbf{q}|h}\end{aligned} \tag{B4}$$

Note that (a) can be proven by conducting a contour integral and using the residue theorem. $\rho_\mathrm{f}(x,y)$ can therefore be expressed as

$$\begin{aligned}\rho_\mathrm{f}(x,y) &= \frac{\mathrm{e}}{L_xL_y}\sum_{k_x,k_y\in\mathbb{Z}}\mathrm{e}^{i(q_xx+q_yy)}\,\mathrm{e}^{-|\mathbf{q}|h} \\ &\overset{\text{(a)}}{=} \frac{\mathrm{e}}{L_xL_y}\sum_{k_x,k_y\in\mathbb{Z}}\cos(q_xx+q_yy)\,\mathrm{e}^{-|\mathbf{q}|h}\end{aligned} \tag{B5}$$

(a) follows from the fact that $\rho_\mathrm{f}(x,y)$ is real-valued and thus $\rho_\mathrm{f}(x,y) = \mathrm{Re}\rho_\mathrm{f}(x,y)$. Equation 4 can thus be obtained by algebraically rearranging eq B5 by noting that the corresponding sum is invariant under inversion. The next step is to obtain the z component of the electric field induced by the charge density given by eq 4

$$\begin{aligned}\tilde{E}_{\mathrm{f},z}^h(0,0,z) &= \frac{2\epsilon_0\epsilon_r(z)L_xL_yE_{\mathrm{f},z}^h(0,0,z)}{\mathrm{e}} \\ &= \frac{h}{2\pi}\int_{-\infty}^{+\infty}\int_{-\infty}^{+\infty}\frac{z\tilde{\rho}_\mathrm{f}(x,y)\,\mathrm{d}x\mathrm{d}y}{[x^2+y^2+z^2]^{3/2}} \\ &\overset{\text{(a)}}{=} 1 + 2\sum_{k=1}^{+\infty}[\mathrm{e}^{-2\pi(z+h)k/L_x} + \mathrm{e}^{-2\pi(z+h)k/L_y}] \\ &\quad + 4\sum_{k_x,k_y=1}^{+\infty}\mathrm{e}^{-2\pi(z+h)\sqrt{\frac{k_x^2}{L_x^2}+\frac{k_y^2}{L_y^2}}}\end{aligned} \tag{B6}$$

Here, ϵ_0 and $\epsilon_\mathrm{r}(z)$ are the vacuum permittivity and the local dielectric constant of the material, respectively. Note that (a) follows from using the following integration identity that can also be proven using the residue theorem

$$\int_{-\infty}^{+\infty}\int_{-\infty}^{+\infty}\frac{\cos\frac{2\pi kx}{L}}{[x^2+y^2+a^2]^{3/2}}\,\mathrm{d}x\,\mathrm{d}y = \frac{2\pi}{a}\,\mathrm{e}^{-2\pi ka/L} \tag{B7}$$

The next step is to integrate eq B6 to obtain the excess change in the electrostatic potential due to the presence of $\tilde{\rho}_\mathrm{f}(x,y)$. More precisely, the excess electrostatic potential, $\Phi^\mathrm{ex}(h)$ is given by

$$\begin{aligned}\tilde{\Phi}^\mathrm{ex}(h) - \tilde{\Phi}^\mathrm{ex}(h_0) &= \frac{2\epsilon_0L_xL_y[\Phi^\mathrm{ex}(h) - \Phi^\mathrm{ex}(h_0)]}{eh} \\ &= \int_{h_0}^{h}\frac{[\tilde{E}_{f,z}^h(0,0,z) - \tilde{E}_{\infty,z}^h(0,0,z)]\,\mathrm{d}z}{h\epsilon_r(z)}\end{aligned} \tag{B8}$$

Here, h_0 is the point at which the anion fully detaches from the conductor and the charge imbalance (resulting in $\rho_\mathrm{f}(x,y)$) is established. In this work, we use $h_0 = 0$, which corresponds to when the leading ion alongside its first hydration shell fully leaves the feed. Assuming that $\epsilon_\mathrm{r}(z) \equiv 1$, which is a reasonable approximation for the interior of the membrane considered in this work, eq B8 can be simplified as

$$\begin{aligned}\tilde{\Phi}^\mathrm{ex}(h) &= \tilde{\Phi}^\mathrm{ex}(h_0) + \frac{h_0}{h} - 1 + \frac{L_x}{\pi h} \\ &\quad \sum_{k=1}^{+\infty}\frac{\mathrm{e}^{-4\pi kh/L_x} - \mathrm{e}^{-2\pi k(h+h_0)/L_x}}{k} \\ &\quad + \frac{L_y}{\pi h}\sum_{k=1}^{+\infty}\frac{\mathrm{e}^{-4\pi kh/L_y} - \mathrm{e}^{-2\pi k(h+h_0)/L_y}}{k} \\ &\quad + \frac{2}{\pi h}\sum_{k_x,k_y=1}^{+\infty}\frac{1}{\sqrt{(k_x/L_x)^2+(k_y/L_y)^2}} \\ &\quad \times [\mathrm{e}^{-4\pi h\sqrt{(k_x/L_x)^2+(k_y/L_y)^2}} \\ &\quad - \mathrm{e}^{-2\pi(h+h_0)\sqrt{(k_x/L_x)^2+(k_y/L_y)^2}}] \\ &\quad + \frac{L_xL_y}{2\pi h}\left[\frac{1}{h_0+h} - \frac{1}{2h}\right]\end{aligned} \tag{B9}$$

The excess electrostatic potential can be used to estimate the correction in free energy given in eq 5.

■ ASSOCIATED CONTENT

Supporting Information

The Supporting Information is available free of charge at https://pubs.acs.org/doi/10.1021/acs.jctc.2c00375.

Induced charge density profiles and mean-squared displacement(PDF)

■ AUTHOR INFORMATION

Corresponding Author

Amir Haji-Akbari − *Department of Chemical and Environmental Engineering, Yale University, New Haven, Connecticut 06520, United States*; orcid.org/0000-0002-2228-6957; Email: amir.hajiakbaribalou@yale.edu

Authors

Brian A. Shoemaker − *Department of Chemical and Environmental Engineering, Yale University, New Haven, Connecticut 06520, United States*

Tiago S. Domingues − *Department of Chemical and Environmental Engineering, Yale University, New Haven, Connecticut 06520, United States*

Complete contact information is available at: https://pubs.acs.org/10.1021/acs.jctc.2c00375

Notes

The authors declare no competing financial interest.

■ ACKNOWLEDGMENTS

A.H.-A. gratefully acknowledges the support of the National Science Foundation Grants CBET-1751971 (CAREER Award) and CBET-2024473. B.S. acknowledges the support of the Goodyear Tire & Rubber Fellowship. We thank P. G. Debenedetti, M. Elimelech, V. Batista, D. Laage, and R.

Coifmann for useful discussions. These calculations were performed on the Yale Center for Research Computing. This work used the Extreme Science and Engineering Discovery Environment (XSEDE), which is supported by National Science Foundation grant no. ACI-1548562.[78]

■ REFERENCES

(1) Matsuura, T.*Synthetic Membranes and Membrane Separation Processes*; CRC Press, 2020.

(2) Werber, J. R.; Deshmukh, A.; Elimelech, M. The critical need for increased selectivity, not increased water permeability, for desalination membranes. *Environ. Sci. Technol. Lett.* **2016**, *3*, 112−120.

(3) Zhou, X.; Wang, Z.; Epsztein, R.; Zhan, C.; Li, W.; Fortner, J. D.; Pham, T. A.; Kim, J.-H.; Elimelech, M. Intrapore energy barriers govern ion transport and selectivity of desalination membranes. *Sci. Adv.* **2020**, *6*, No. eabd9045.

(4) Epsztein, R.; DuChanois, R. M.; Ritt, C. L.; Noy, A.; Elimelech, M. Towards single-species selectivity of membranes with subnanometre pores. *Nat. Nanotechnol.* **2020**, *15*, 426−436.

(5) Heiranian, M.; Farimani, A. B.; Aluru, N. R. Water desalination with a single-layer MoS_2 nanopore. *Nat. Commun.* **2015**, *6*, 8616.

(6) Cohen-Tanugi, D.; Lin, L.-C.; Grossman, J. C. Multilayer Nanoporous Graphene Membranes for Water Desalination. *Nano Lett.* **2016**, *16*, 1027−1033.

(7) Yan, Y.; Wang, W.; Li, W.; Loh, K.; Zhang, J. A graphene-like membrane with an ultrahigh water flux for desalination. *Nanoscale* **2017**, *9*, 18951−18958.

(8) Zhang, Y.; Fang, T.; Hou, Q.; Li, Z.; Yan, Y. Water desalination of a new three-dimensional covalent organic framework: A molecular dynamics simulation study. *Phys. Chem. Chem. Phys.* **2020**, *22*, 16978−16984.

(9) Hussain, S.; Haji-Akbari, A. Studying rare events using forward-flux sampling: Recent breakthroughs and future outlook. *J. Chem. Phys.* **2020**, *152*, 060901.

(10) Malmir, H.; Epsztein, R.; Elimelech, M.; Haji-Akbari, A. Induced charge anisotropy: A hidden variable affecting ion transport through membranes. *Matter* **2020**, *2*, 735−750.

(11) Gupta, R.; Badhe, Y.; Mitragotri, S.; Rai, B. Permeation of nanoparticles across the intestinal lipid membrane: Dependence on shape and surface chemistry studied through molecular simulations. *Nanoscale* **2020**, *12*, 6318−6333.

(12) Cohen-Tanugi, D.; Grossman, J. C. Water desalination across nanoporous graphene. *Nano Lett.* **2012**, *12*, 3602−3608.

(13) Haji-Akbari, A. Forward-flux sampling with jumpy order parameters. *J. Chem. Phys.* **2018**, *149*, 072303.

(14) Binder, K. Finite size effects on phase transitions. *Ferroelectrics* **1987**, *73*, 43−67.

(15) Mon, K.; Binder, K. Finite size effects for the simulation of phase coexistence in the Gibbs ensemble near the critical point. *J. Chem. Phys.* **1992**, *96*, 6989−6995.

(16) Horbach, J.; Kob, W.; Binder, K.; Angell, C. A. Finite size effects in simulations of glass dynamics. *Phys. Rev. E: Stat. Phys., Plasmas, Fluids, Relat. Interdiscip. Top.* **1996**, *54*, R5897.

(17) Aguado, A.; Scott, W.; Madden, P. A. Molecular dynamics simulations of the liquid−vapor interface of a molten salt. II. Finite size effects and comparison to experiment. *J. Chem. Phys.* **2001**, *115*, 8612−8619.

(18) Orea, P.; López-Lemus, J.; Alejandre, J. Oscillatory surface tension due to finite-size effects. *J. Chem. Phys.* **2005**, *123*, 114702.

(19) Mastny, E. A.; de Pablo, J. J. Melting line of the Lennard-Jones system, infinite size, and full potential. *J. Chem. Phys.* **2007**, *127*, 104504.

(20) Biscay, F.; Ghoufi, A.; Goujon, F.; Lachet, V.; Malfreyt, P. Calculation of the surface tension from Monte Carlo simulations: Does the model impact on the finite-size effects? *J. Chem. Phys.* **2009**, *130*, 184710.

(21) Burt, R.; Birkett, G.; Salanne, M.; Zhao, X. Molecular dynamics simulations of the influence of drop size and surface potential on the contact angle of ionic-liquid droplets. *J. Phys. Chem. C* **2016**, *120*, 15244−15250.

(22) Salacuse, J.; Denton, A.; Egelstaff, P. Finite-size effects in molecular dynamics simulations: Static structure factor and compressibility. I. Theoretical method. *Phys. Rev. E: Stat. Phys., Plasmas, Fluids, Relat. Interdiscip. Top.* **1996**, *53*, 2382.

(23) Yeh, I.-C.; Hummer, G. System-size dependence of diffusion coefficients and viscosities from molecular dynamics simulations with periodic boundary conditions. *J. Phys. Chem. B* **2004**, *108*, 15873−15879.

(24) Botan, A.; Marry, V.; Rotenberg, B. Diffusion in bulk liquids: Finite-size effects in anisotropic systems. *Mol. Phys.* **2015**, *113*, 2674−2679.

(25) Jamali, S. H.; Wolff, L.; Becker, T. M.; Bardow, A.; Vlugt, T. J.; Moultos, O. A. Finite-size effects of binary mutual diffusion coefficients from molecular dynamics. *J. Chem. Theory Comput.* **2018**, *14*, 2667−2677.

(26) Hussain, S.; Haji-Akbari, A. How to quantify and avoid finite size effects in computational studies of crystal nucleation: The case of heterogeneous ice nucleation. *J. Chem. Phys.* **2021**, *154*, 014108.

(27) Hussain, S.; Haji-Akbari, A. How to quantify and avoid finite size effects in computational studies of crystal nucleation: The case of homogeneous crystal nucleation. *J. Chem. Phys.* **2022**, *156*, 054503.

(28) Frisch, M. J.; Trucks, G. W.; Schlegel, H. B.; Scuseria, G. E.; Robb, M. A.; Cheeseman, J. R.; Scalmani, G.; Barone, V.; Petersson, G. A.; Nakatsuji, H.; Li, X.; Caricato, M.; Marenich, A. V.; Bloino, J.; Janesko, B. G.; Gomperts, R.; Mennucci, B.; Hratchian, H. P.; Ortiz, J. V.; Izmaylov, A. F.; Sonnenberg, J. L.; Williams-Young, D.; Ding, F.; Lipparini, F.; Egidi, F.; Goings, J.; Peng, B.; Petrone, A.; Henderson, T.; Ranasinghe, D.; Zakrzewski, V. G.; Gao, J.; Rega, N.; Zheng, G.; Liang, W.; Hada, M.; Ehara, M.; Toyota, K.; Fukuda, R.; Hasegawa, J.; Ishida, M.; Nakajima, T.; Honda, Y.; Kitao, O.; Nakai, H.; Vreven, T.; Throssell, K.; Montgomery, J. A., Jr.; Peralta, J. E.; Ogliaro, F.; Bearpark, M. J.; Heyd, J. J.; Brothers, E. N.; Kudin, K. N.; Staroverov, V. N.; Keith, T. A.; Kobayashi, R.; Normand, J.; Raghavachari, K.; Rendell, A. P.; Burant, J. C.; Iyengar, S. S.; Tomasi, J.; Cossi, M.; Millam, J. M.; Klene, M.; Adamo, C.; Cammi, R.; Ochterski, J. W.; Martin, R. L.; Morokuma, K.; Farkas, O.; Foresman, J. B.; Fox, D. J.*Gaussian 16* Revision C. 01. 2016; Gaussian Inc.: Wallingford CT, 2016; p 421.

(29) Tirado-Rives, J.; Jorgensen, W. L. Performance of B3LYP density functional methods for a large set of organic molecules. *J. Chem. Theory Comput.* **2008**, *4*, 297−306.

(30) Hehre, W. J.; Stewart, R. F.; Pople, J. A. Self-consistent molecular-orbital methods. I. Use of gaussian expansions of slater-type atomic orbitals. *J. Chem. Phys.* **1969**, *51*, 2657−2664.

(31) Humphrey, W.; Dalke, A.; Schulten, K. VMD—Visual Molecular Dynamics. *J. Mol. Graphics* **1996**, *14*, 33−38.

(32) Allouche, A.-R. Gabedit—A Graphical User Interface for Computational Chemistry Softwares. *J. Comput. Chem.* **2012**, *32*, 174−182.

(33) Plimpton, S. Short-Range Molecular Dynamics. *J. Comput. Phys.* **1995**, *117*, 1−42.

(34) Price, D. J.; Brooks, C. L. A modified TIP3P water potential for simulation with Ewald summation. *J. Chem. Phys.* **2004**, *121*, 10096−10103.

(35) Joung, I. S.; Cheatham, T. E. Determination of alkali and halide monovalent ion parameters for use in explicitly solvated biomolecular simulations. *J. Phys. Chem. B* **2008**, *112*, 9020−9041.

(36) Müller-Plathe, F. Local structure and dynamics in solvent-swollen polymers. *Macromolecules* **1996**, *29*, 4782−4791.

(37) Beu, T. A. Molecular dynamics simulations of ion transport through carbon nanotubes. I. Influence of geometry, ion specificity, and many-body interactions. *J. Chem. Phys.* **2010**, *132*, 164513.

(38) Swope, W. C.; Andersen, H. C.; Berens, P. H.; Wilson, K. R. A computer simulation method for the calculation of equilibrium constants for the formation of physical clusters of molecules: Application to small water clusters. *J. Chem. Phys.* **1982**, *76*, 637−649.

(39) Nosé, S. A molecular dynamics method for simulations in the canonical ensemble. *Mol. Phys.* **1984**, *52*, 255−268.

(40) Hoover, W. G. Canonical dynamics: Equilibrium phase-space distributions. *Phys. Rev. A: At., Mol., Opt. Phys.* **1985**, *31*, 1695−1697.

(41) Evans, D.; Holian, B. The Nose−Hoover thermostat. *J. Chem. Phys.* **1985**, *83*, 4069−4074.

(42) Andersen, H. C. Rattle: A "velocity" version of the shake algorithm for molecular dynamics calculations. *J. Comput. Phys.* **1983**, *52*, 24−34.

(43) Hockney, R. W.; Eastwood, J. W.*Computer Simulation Using Particles*; Hilger: Bristol, 1988; p 1988.

(44) Bostick, D.; Berkowitz, M. L. The implementation of slab geometry for membrane-channel molecular dynamics simulations. *Biophys. J.* **2003**, *85*, 97−107.

(45) Allen, R. J.; Frenkel, D.; ten Wolde, P. R. Simulating rare events in equilibrium or nonequilibrium stochastic systems. *J. Chem. Phys.* **2006**, *124*, 024102.

(46) Valeriani, C.; Sanz, E.; Frenkel, D. Rate of homogeneous crystal nucleation in molten NaCl. *J. Chem. Phys.* **2005**, *122*, 194501.

(47) Li, T.; Donadio, D.; Ghiringhelli, L. M.; Galli, G. Surface-induced crystallization in supercooled tetrahedral liquids. *Nat. Mater.* **2009**, *8*, 726−730.

(48) Li, T.; Donadio, D.; Russo, G.; Galli, G. Homogeneous ice nucleation from supercooled water. *Phys. Chem. Chem. Phys.* **2011**, *13*, 19807−19813.

(49) Thapar, V.; Escobedo, F. A. Localized orientational order chaperones the nucleation of rotator phases in hard polyhedral particles. *Phys. Rev. Lett.* **2014**, *112*, 048301.

(50) Haji-Akbari, A.; DeFever, R. S.; Sarupria, S.; Debenedetti, P. G. Suppression of sub-surface freezing in free-standing thin films of a coarse-grained model of water. *Phys. Chem. Chem. Phys.* **2014**, *16*, 25916−25927.

(51) Haji-Akbari, A.; Debenedetti, P. G. Direct calculation of ice homogeneous nucleation rate for a molecular model of water. *Proc. Natl. Acad. Sci. U.S.A.* **2015**, *112*, 10582.

(52) Bi, Y.; Cabriolu, R.; Li, T. Heterogeneous ice nucleation controlled by the coupling of surface crystallinity and surface hydrophilicity. *J. Phys. Chem. C* **2016**, *120*, 1507−1514.

(53) Bi, Y.; Cao, B.; Li, T. Enhanced heterogeneous ice nucleation by special surface geometry. *Nat. Commun.* **2017**, *8*, 15372.

(54) Haji-Akbari, A.; Debenedetti, P. G. Computational investigation of surface freezing in a molecular model of water. *Proc. Natl. Acad. Sci. U.S.A.* **2017**, *114*, 3316−3321.

(55) Sosso, G. C.; Whale, T. F.; Holden, M. A.; Pedevilla, P.; Murray, B. J.; Michaelides, A. Unravelling the origins of ice nucleation on organic crystals. *Chem. Sci.* **2018**, *9*, 8077−8088.

(56) Hussain, S.; Haji-Akbari, A. Role of nanoscale interfacial proximity in contact freezing in water. *J. Am. Chem. Soc.* **2021**, *143*, 2272−2284.

(57) Sharma, S.; Debenedetti, P. G. Evaporation rate of water in hydrophobic confinement. *Proc. Natl. Acad. Sci. U.S.A.* **2012**, *109*, 4365−4370.

(58) Altabet, Y. E.; Haji-Akbari, A.; Debenedetti, P. G. Effect of material flexibility on the thermodynamics and kinetics of hydrophobically induced evaporation of water. *Proc. Natl. Acad. Sci. U.S.A.* **2017**, *114*, E2548−E2555.

(59) Borrero, E. E.; Escobedo, F. A. Folding kinetics of a lattice protein via a forward flux sampling approach. *J. Chem. Phys.* **2006**, *125*, 164904.

(60) Richard, D.; Löwen, H.; Speck, T. Nucleation pathway and kinetics of phase-separating active Brownian particles. *Soft Matter* **2016**, *12*, 5257−5264.

(61) Li, Y.; ten Wolde, P. R. Shape transformations of vesicles induced by swim pressure. *Phys. Rev. Lett.* **2019**, *123*, 148003.

(62) Goncharov, A. F.; Goldman, N.; Fried, L. E.; Crowhurst, J. C.; Kuo, I.-F. W.; Mundy, C. J.; Zaug, J. M. Dynamic ionization of water under extreme conditions. *Phys. Rev. Lett.* **2005**, *94*, 125508.

(63) Hernández-Ortiz, J. P.; Chopra, M.; Geier, S.; de Pablo, J. J. Hydrodynamic effects on the translocation rate of a polymer through a pore. *J. Chem. Phys.* **2009**, *131*, 044904.

(64) Thapar, V.; Escobedo, F. A. Simultaneous estimation of free energies and rates using forward flux sampling and mean first passage times. *J. Chem. Phys.* **2015**, *143*, 244113.

(65) Peters, B.*Reaction Rate Theory and Rare Events*; Elsevier, 2017.

(66) Kramers, H. A. Brownian motion in a field of force and the diffusion model of chemical reactions. *Phys. A* **1940**, *7*, 284−304.

(67) Langer, J. S. Statistical theory of the decay of metastable states. *Ann. Phys.* **1969**, *54*, 258−275.

(68) Childress, A. E.; Elimelech, M. Relating nanofiltration membrane performance to membrane charge (electrokinetic) characteristics. *Environ. Sci. Technol.* **2000**, *34*, 3710−3716.

(69) Epsztein, R.; Shaulsky, E.; Dizge, N.; Warsinger, D. M.; Elimelech, M. Role of Ionic charge density in Donnan exclusion of monovalent anions by nanofiltration. *Environ. Sci. Technol.* **2018**, *52*, 4108−4116.

(70) Pang, R.; Zhang, K. Fabrication of hydrophobic fluorinated silica-polyamide thin film nanocomposite reverse osmosis membranes with dramatically improved salt rejection. *J. Colloid Interface Sci.* **2018**, *510*, 127−132.

(71) Li, Y.; Yang, S.; Zhang, K.; Van der Bruggen, B. Thin film nanocomposite reverse osmosis membrane modified by two dimensional laminar MoS_2 with improved desalination performance and fouling-resistant characteristics. *Desalination* **2019**, *454*, 48−58.

(72) Yao, Y.; Zhang, P.; Jiang, C.; DuChanois, R. M.; Zhang, X.; Elimelech, M. High performance polyester reverse osmosis desalination membrane with chlorine resistance. *Nat. Sustain.* **2021**, *4*, 138−146.

(73) Lee, K. P.; Arnot, T. C.; Mattia, D. A review of reverse osmosis membrane materials for desalination—Development to date and future potential. *J. Membr. Sci.* **2011**, *370*, 1−22.

(74) Schlaich, A.; Knapp, E. W.; Netz, R. R. Water dielectric effects in planar confinement. *Phys. Rev. Lett.* **2016**, *117*, 048001.

(75) Fumagalli, L.; Esfandiar, A.; Fabregas, R.; Hu, S.; Ares, P.; Janardanan, A.; Yang, Q.; Radha, B.; Taniguchi, T.; Watanabe, K.; Gomila, G.; Novoselov, K. S.; Geim, A. K. Anomalously low dielectric constant of confined water. *Science* **2018**, *360*, 1339−1342.

(76) Olivieri, J.-F.; Hynes, J. T.; Laage, D. Confined water's dielectric constant reduction is due to the surrounding low dielectric media and not to interfacial molecular ordering. *J. Phys. Chem. Lett.* **2021**, *12*, 4319−4326.

(77) Ngo, V.; Li, H.; MacKerell, A. D., Jr; Allen, T. W.; Roux, B.; Noskov, S. Polarization effects in water-mediated selective cation transport across a narrow transmembrane channel. *J. Chem. Theory Comput.* **2021**, *17*, 1726−1741.

(78) Towns, J.; Cockerill, T.; Dahan, M.; Foster, I.; Gaither, K.; Grimshaw, A.; Hazlewood, V.; Lathrop, S.; Lifka, D.; Peterson, G. D.; Roskies, R.; Scott, J. R.; Wilkins-Diehr, N. XSEDE: Accelerating Scientific Discovery. *Comput. Sci. Eng.* **2014**, *16*, 62−74.

(79) Stein, E. M.; Shakarchi, R.*Fourier Analysis: An Introduction*; Princeton University Press, 2011; Vol. *1*.